JET–R(99)07

L C Ingesson

Application of Natural Basis Functions to Soft X-ray Tomography

JET–R(99)07

Application of Natural Basis Functions to Soft X-ray Tomography

L C Ingesson.

JET Joint Undertaking, Abingdon, Oxfordshire, OX14 3EA, UK.

March 2000

ABSTRACT

Natural basis functions (NBFs), also known as natural pixels in the literature, have been applied in tomographic reconstructions of simulated measurements for the JET soft x-ray system, which has a total of about 200 detectors spread over 6 directions. Various types of NBFs, i.e. normal, generalized and orthonormal NBFs, are reviewed. The number of basis functions is roughly equal to the number of measurements. Therefore, little *a priori* information is required as regularization and truncated singular-value decomposition can be used for the tomographic inversion. The results of NBFs are compared with reconstructions by the same solution technique using local basis functions (LBFs), and with the reconstructions of a conventional constrained-optimization tomography method with many more LBFs that requires more *a priori* information. Although the results of the conventional method are superior due to the *a priori* information, the results of the NBF and other LBF methods are reasonable and show the main features. Therefore, NBFs are a promising way to assess whether features in reconstructions are real or artefacts resulting from the *a priori* information. Of the NBFs, regular triangular (generalized) NBFs give the most acceptable reconstructions, much better than traditional square pixels, although the reconstructions with pyramid-shaped LBFs are also reasonable and have slightly smaller reconstruction errors. A more-regular (virtual) viewing geometry improves the reconstructions. However, simulations with a viewing geometry with a total of 480 channels spread over 12 directions clearly show that *a priori* information still improves the reconstructions considerably.

1. INTRODUCTION

Emission tomography, in which the local emission is reconstructed from a large number of measurements along narrow strips through an emitting plasma, is a typical tomographic problem occurring in fusion research. In this report two-dimensional emission tomography without refraction and re-absorption of radiation is assumed, but the results should be relevant for other applications as well. Virtually all methods for tomographic reconstruction applied in fusion research are so-called series-expansion methods. In these methods the mathematical description of the measurement process is discretized, after which the problem is inverted. This is contrary to so-called transform methods where the problem is first inverted and only then discretized [1]. The latter methods are generally more efficient and in wide use in medical tomography, but they are less general because usually they require a regular coverage, they assume the measurements to be along infinitely thin lines, and they exclude the application of *a priori* knowledge about the expected emission profiles. Due to the restricted access to fusion devices, in fusion research there are usually relatively few measurements from a few irregularly distributed directions. Furthermore, to obtain a sufficient signal-to-noise ratio the measurements are along relatively wide strips. Although there are ways to overcome these two problems with transform methods, see for example Refs. 2 and 3, it is much easier in series-expansion methods. Furthermore, in

series-expansion methods it is more straightforward to take into account *a priori* information and other physical effects such as re-absorption, scatter, refraction, etc.

In series-expansion methods the emission profile (in the case of emission tomography) is discretized by expanding it on a set of basis functions. Basis functions can either be local or global [4]. Regularized series-expansion methods can cope with various local or global basis functions, see for instance Ref. 5.[1] Examples of global basis functions applied in tomography in fusion research are the Fourier-Zernike [6] and Fourier-Bessel [7] expansions of the Cormack method. Local basis functions (LBFs) include the much-used pixels [8–10] and related functions describing a small region on a regular grid [4,11,12]. Global basis functions have a restricted application because a limited number of the functions have to describe the emission profile well, while local basis functions are much more flexible because *a priori* information can easily be implemented. Natural basis functions (NBFs), often referred to as natural pixels in the literature, were proposed by McCaughey and Andrews [13] and Buonocore *et al.* [14] as global basis functions that in certain tomography problems are well suited as a replacement of LBFs. NBFs are related to the strips with finite width that are viewed by the measuring system, and are therefore in a certain sense ideally suited to describe the measurements by that system [14]. Recently, NBFs have been applied successfully in single positron emission computed tomography (SPECT) [15,16], in which a tomographic image is formed of the emission from radionuclides injected into a patient. A similarity between SPECT and tomography in fusion research is that the beam widths of the imaging system are relatively large in order to achieve a good signal-to-noise ratio. An important dissimilarity is that many more measurements from a regular coverage are available in SPECT. However, in modern soft x-ray tomography diagnostics on fusion devices there may be sufficient information (number of measurements) to make reasonable reconstructions by means of NBF methods without *a priori* information.[2] The purpose of this report is to investigate whether this is the case and to discuss the advantages and disadvantages of NBF methods compared with other tomography methods with LBFs. A number of types of NBFs are investigated: the original NBFs [14], generalized NBFs [17], and orthonormal NBFs [18].

Examples of the NBFs are given for the soft x-ray (SXR) system on the JET tokamak. The assessment, by simulations, of the performance of tomography methods with the various NBFs and LBFs is done for the same system. The JET SXR system consists of $5^1/_2$ nearly complete views of the plasma with 35 or 36 channels each [Fig.1(a)]. To assess whether the results would be different for systems with a more regular and complete coverage, simulations were also carried out for two virtual systems with 6×40 and 12×40 channels, respectively [Fig.1(b)].

---

[1] The regularization in Ref. 5 is smoothness of the expansion coefficients for both local and global basis functions. In general, however, smoothness cannot be used for global basis functions. For global basis functions a rough regularization is often achieved by truncating the series expansion, see Sec. 2.4 and, for example, Ref. 6.

[2] In this report the statement "without *a priori* information" means without *a priori* information such as smoothness and other assumed properties of the emission profile. Even NBF methods require regularization in the form of the estimated noise in the measurement, which in a strict sense can also be called *a priori* information.

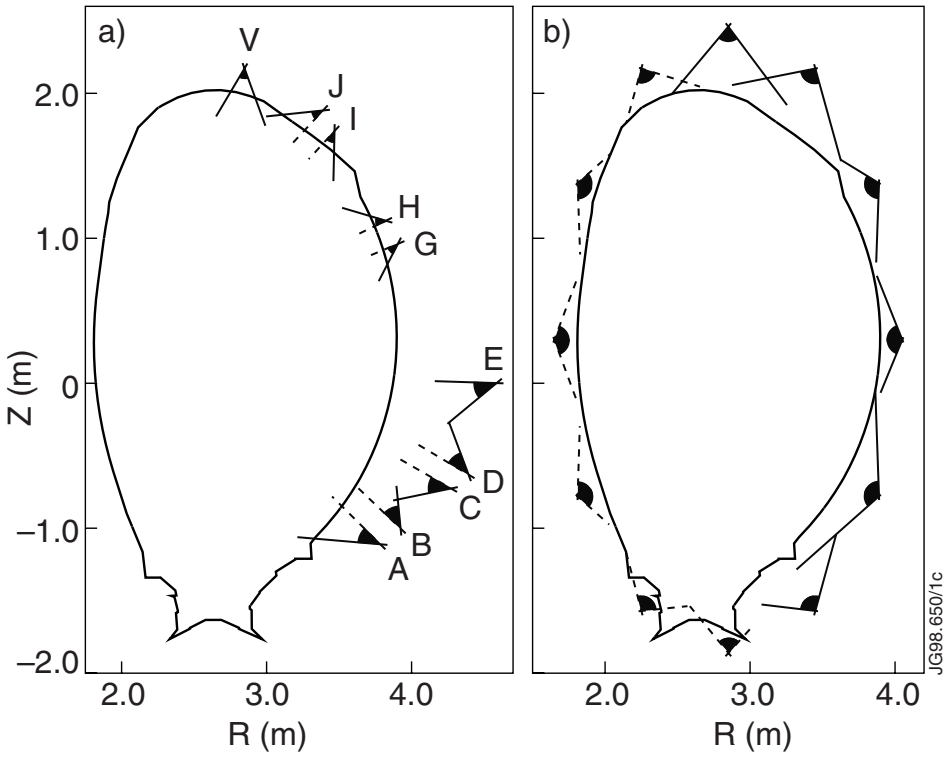

Fig.1: (a) Extent of the viewing fans of the JET SXR system. Eight detector arrays with 18 channels are grouped in pairs to give nearly complete views of the plasma (AB, CD, GH, and IJ), one array (E, 18 channels) views half of the plasma, and one array (V, 35 channels) has a wider view. (b) Extent of the viewing fans of measuring systems with complete coverage (40 channels per fan) and fans at regularly spaced angles. Simulations were done with the six outside fans (solid lines), and with all 12 fans (solid and dashed lines).

The structure of this report is as follows. Section 2 introduces the various NBFs and LBFs and describes the numerical implementation of the tomography methods. Section 3 discusses the results of simulations to compare the tomography methods using the various basis functions, and Sec. 4 summarizes the results.

2. MATHEMATICAL BACKGROUND

2.1 Series-expansion methods

In series-expansion methods the emission profile $g(x,y)$, where x and y are the spatial Cartesian coordinates, is expanded on a set of basis functions $B_j(x,y)$:

$$g(x,y) \approx \sum\nolimits_j B_j(x,y)\,\tilde{g}_j\,. \tag{1}$$

Later, the xy coordinates will be identified with the coordinates of a poloidal tokamak cross-section R and Z, respectively, and will be used interchangeably with these. The measurement of detector i can be written as

$$f_i = \{\mathrm{K}g(x,y)\}_i = \iint K_i(x,y)\,g(x,y)\,\mathrm{d}x\,\mathrm{d}y\,, \tag{2}$$

where the integral is over the support of $g(x,y)$, which is assumed to be bounded. Here, a discrete-continuous integral operator $\mathbf{K}$ that maps the continuous function $g(x,y)$ in $\mathbf{R}^2$ to the discrete

measurements f_i has been introduced. The kernel $K_i(x,y)$ describes the geometric properties of the measuring system and will be referred to as the geometric function.[3] The function $K_i(x,y)$ is non-zero in a strip-shaped region [see Fig.2(a) for an example] and Eq.(2) can sometimes be approximated by a strip integral. Substituting Eq.(1) into Eq.(2) gives the matrix equation

$$\boldsymbol{f} = A\tilde{\boldsymbol{g}}\,, \tag{3}$$

where $\boldsymbol{f}$ and $\tilde{\boldsymbol{g}}$ are vectors with elements f_i and $\tilde{g}_j$, respectively, and the matrix elements are given by

$$A_{ij} = \iint K_i(x,y)\, B_j(x,y)\,\mathrm{d}x\,\mathrm{d}y\,. \tag{4}$$

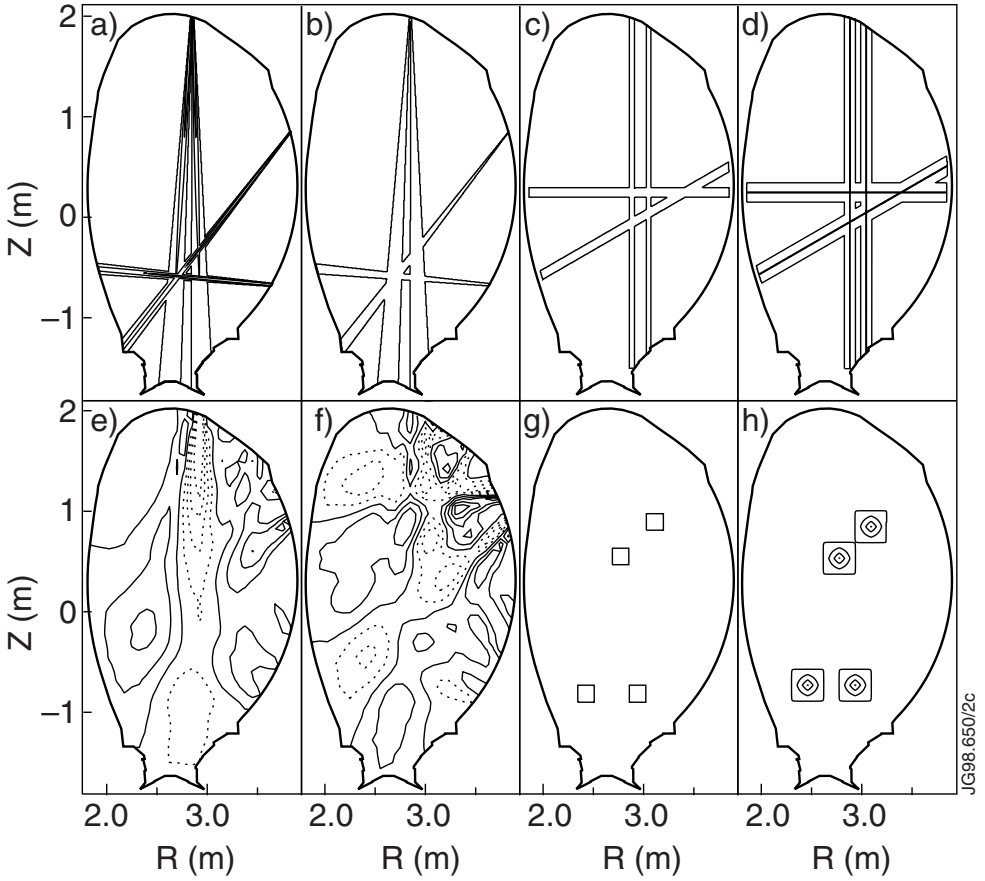

Fig.2: Contour plots of various typical basis functions. The NBFs are based on the geometry of the SXR system at JET and are shown with respect to the inner wall of the JET tokamak. (a) Four standard NBFs B^1, equal to $K_i(x,y)$. (b) Four support NBFs B^2. (c) Four constant regular NBFs B^3. (d) Four triangular regular NBFs B^4. (e,f) Two orthonormal NBFs B^5 (dotted contours indicate negative values). (g) Four square constant LBFs B^6. (h) Four pyramid LBFs B^7. Neighbouring basis functions were not drawn; note however that neighbouring basis functions in (d) and (h) overlap, and also in (a) and (b) in so far as $K_i(x,y)$ of neighbouring channels overlap. The representation of the basis functions in (a–d,g,h) is on the fine 400×800 grid, whereas (e,f) are on a coarser grid.

[3] Another name for the geometric function regularly used in the literature is (point) response function; if the operator **K** is continuous-continuous, the corresponding kernel is often referred to as the point spread function. Note that the name point spread function is sometimes used with a different meaning in tomography, namely the inverse Radon transform of the geometric function.

Basis functions used in various tomography methods can be divided into the groups mentioned in the Introduction. *Local basis functions* are functions with a support (i.e. region where they are not zero) that is much smaller than the support of the function $g(x,y)$. A well-known example of LBFs are square pixels, where $B_j(x,y)$ is 1 inside pixel j and 0 outside. Other LBFs [4,11] are overlapping triangular functions that guarantee that the expansion Eq. (1) gives a continuous result [see Fig.2(h) for an example], and spline functions that guarantee it to have continuous first derivatives. When the support of each basis function covers a large part of the support of $g(x,y)$, the basis functions are called *global*. This is the case when basis functions linearly model physical or mathematical properties of the emission profile [if the model is not linear Eq.(1) is not valid], or when they model the detection system. An example of the former is the Cormack method, mentioned in the introduction, that has been useful in fusion research to study, for example, MHD modes. NBFs are a way to model the detection system.

If the basis functions form an orthogonal set, a unique expansion Eq.(1) is guaranteed and the expansion coefficients can be determined from $\tilde{g}_j = \langle g(x,y) | B_j(x,y) \rangle$, where the brackets denote the scalar product in Dirac notation. This is the case with several types of LBFs, such as square pixels, and some mathematical global basis functions, such as the ones used in the Cormack method. If the set of basis functions is not orthogonal, Eq.(1) may still describe a unique expansion, i.e. one can solve Eq.(1) for given $g(x,y)$ and basis functions to find $\tilde{\boldsymbol{g}}$. However, solving Eq.(1) is generally not required in tomography because $g(x,y)$ is the unknown: Eq.(3) is solved to find $\tilde{\boldsymbol{g}}$ from the measurements $\boldsymbol{f}$, after which an approximate $g(x,y)$ is found by substituting the found $\tilde{\boldsymbol{g}}$ in Eq.(1).

If Eq. (3) is overdetermined, i.e. there are more (known) measurements that (unknown) basis-function expansion coefficients, there may be a unique solution. However, in the presence of noise and inconsistencies in the data it is likely that there is no exact solution. It is well known that the tomography problem is a so-called ill-posed problem [19]: it is easy to see that the integral Eq.(2) averages over variations in $g(x,y)$ and hence the inverse will amplify noise in the measurements $\boldsymbol{f}$ [20]. In the overdetermined case a least-squares solution may be adequate. However, often more expansion coefficients $\tilde{g}_j$ are required than there are measurements f_i, so that Eq.(3) is underdetermined. Then, no unique solution exists and one has to regularize the inverse problem, for example by taking into account *a priori* information. Possible regularizations include truncated singular value decomposition, smoothness, flatness, maximum entropy, non-negativity, and zeroness of emissivity outside the plasma, some of which will be discussed later.

2.2 Natural basis functions

The most straightforward choice of NBFs, which will be referred to as *standard* NBFs, is [14]

$$B_j(x,y) = K_j(x,y). \tag{5}$$

With this choice Eqs.(1) and (2) become very symmetrical, and, in fact, Eq.(1) can be written as

$$g(x,y) = \mathtt{K}^{\dagger}\tilde{\boldsymbol{g}}, \tag{6}$$

where $\mathtt{K}^{\dagger}$ is the adjoint operator of $\mathbf{K}$. This will be shown in matrix notation in section 2.3. If one, as is customary in the tomography field, refers to the strip-like integral of Eq.(2) as *projection*, with the choice of NBFs one can refer to Eqs.(1) and (6) as the *backprojection*. Indeed, Eq.(1) is closely related to a discrete version of the continuous backprojection operator of which the continuous form is well known in transform methods [1].[4] For obvious reasons, the matrix $A = \mathtt{K}\mathtt{K}^{\dagger}$ is sometimes referred to as the projection-backprojection matrix.

With the choice of basis functions of Eq.(5) the number of expansion coefficients $\tilde{g}_j$ is equal to the number of measurements, so that Eq.(3) may have a unique solution. Ways of solving Eq.(3) are discussed in section 2.4. A major advantage of NBF methods is that they can be much more computationally efficient than LBF methods that usually have many more expansion coefficients than measurements.[5] A further advantage is that NBFs represent the information in the measurements well. Disadvantages are that for arbitrary systems there is no way to take into account *a priori* information with standard NBFs and that the measurements alone may not be sufficient to accurately describe the emission profile. Although Buonocore *et al.* [14] claim that natural basis functions are optimal for tomographic reconstructions of actual objects (in fact, they mean that natural basis functions give smaller discretization errors than square pixels), it is more relevant to consider in how far the various basis functions can describe the object. Hanson *et al.* [4,21] argue that only the information about $g(x,y)$ that lies in the subspace (called measurement space) spanned by the set of all geometric functions is contained in the measurements, and no information about the orthogonal space (called null space). This is true for any basis functions; *a priori* information is required to fill the null space. Because natural basis functions can only represent the information in the measurement space, *a priori* information cannot be added. For a regular coverage this may not be such a problem, but for irregular coverage a significant null space may exist.

---

[4] In the filtered-backprojection (FBP) method (also known as convolution-backprojection), one of the most widely applied transform methods, a filtering operation is carried out on the measurements before backprojecting them [1]. With B chosen as in Eq. (5) for a viewing system in which the geometric function describes parallel strip integrals, solving $\tilde{\boldsymbol{g}}$ from Eq. (3) must therefore be a discrete equivalent of the filtering operation in FBP.

[5] Here it is meant that NBF methods are more efficient than LBF methods that use the same solution technique, simply because the matrix size is smaller for NBF methods if there are more grid points than measurements, i.e. in NBF methods Eq. (3) is solved, whereas in normal NBF methods a discrete version of Eq. (2) is solved. In this report a matrix inversion is obtained by means of truncated singular value decomposition, which is feasible on present-day computers for matrix dimensions of several thousand. For larger matrices iterative techniques, such as ART-like algorithms [algebraic reconstruction technique, see for instance Herman G T 1980 *Image reconstruction from projections* (New York: Academic Press) pp 180] have to be employed, which can be efficient and achieve acceptable solutions for systems with good coverage. See Sec. 2.4 for a further discussion.

One is free in the choice of basis functions, so one can choose the backprojection to use the backprojection operator (basis functions) of another measuring geometry [$K'_j(x,y)$] than in the projection, i.e.

$$B_j(x,y) = K'_j(x,y) \neq K_j(x,y). \tag{7}$$

Such basis functions have been referred too as *generalized* NBFs [17]. These NBFs may be advantageous if the coverage of the measuring system is irregular or truncated, in which case $K'_j(x,y)$ may be chosen to represent a (virtual) full regular measuring system, which has a smaller null space than the actual measuring system. Note that in this case the matrix *A* need not be square since the irregular and regular measuring systems may have different numbers of detectors. One can also orthonormalize the NBFs [13,18], which leads to *orthonormal* NBFs. These NBFs are discussed in detail in the section 2.3.

If the imaging system can be approximated by strip integrals, i.e. $K_i(x,y)$ equals 1 inside the strip and 0 everywhere else, the matrix *A* of Eq.(4) for standard or generalized NBFs can be calculated analytically because A_{ij} is simply the area of intersection between strips *i* and *j* [15,17]. The only need for discretization of the continuous description in that case is the backprojection Eq.(1), to obtain a discrete image of the emission profile. In many actual measuring systems the width of the strips varies with distance from the detector, and, consequently [3], the value of $K_i(x,y)$ decreases with distance. In such more complicated imaging systems [see for example Fig.2(a)] the representation of $K_i(x,y)$ has to be discretized. Although in this case still a continuous mathematical description is possible until the numerical implementation, see Ref. 18, it requires the introduction of new notation for discrete-continuous operators. By discretizing the problem from the start, a consistent description of all methods is obtained and the way to implement the methods numerically is evident, as is discussed next.

2.3 Numerical implementation of basis functions

In the numerical implementation one discretizes the geometric function $K_i(x,y)$ with strictly local basis functions $b_m(x,y)$, for example *M* small pixels. Note that a lower case *b* is used for these LBFs of the numerical implementation to distinguish them from the basis functions *B* of the tomography method. These LBFs of the numerical implementation are referred to here as *grid* LBFs. The discrete representation g_m of the emission profile $g(x,y)$ on this set of grid basis functions is given by the expansion

$$g(x,y) \approx \sum\nolimits_m b_m(x,y)\, g_m\,; \tag{8}$$

note that there is no tilde on these expansion coefficients g_m, which for square pixels corresponds to the average emissivity in small pixel *m*. The geometric matrix, i.e. the discrete representation K_{im} of the geometric function, is given by

$$K_{im} = \iint K_i(x,y)\, b_m(x,y)\, \mathrm{d}x\, \mathrm{d}y, \tag{9}$$

and, similarly, the discrete representation of the basis functions $B_j(x,y)$ by B_{jm}:

$$B_{jm} = \iint B_j(x,y)\, b_m(x,y)\, \mathrm{d}x\, \mathrm{d}y. \tag{10}$$

Using Eq.(10), one can give the discrete expression for the local emissivities

$$g_m \approx \sum\nolimits_j B_{jm}\, \tilde{g}_j \text{, or } \boldsymbol{g} \approx B^{\mathsf{T}} \tilde{\boldsymbol{g}}. \tag{11}$$

The projection-backprojection matrix A of Eq. (3) in terms of the matrices K and B is $A = K\,B^{\mathsf{T}}$. Equation (2) expressed in matrix form is

$$\boldsymbol{f}=K\boldsymbol{g}. \tag{12}$$

Various types of basis functions are introduced, a graphical representation of which is given in Fig.2 for the JET SXR system. In the following it is assumed that there are I detectors and J basis functions. The standard NBFs ($J = I$) are given by

$$B^1 = K. \tag{13}$$

With this choice, Eq.(11) justifies Eq.(6). A contour plot of a collection of these basis functions is shown in Fig.2(a). The contours indicate strongly varying values of B^1 inside the strips on their support (i.e. the region where they are non-zero). This is the reason why in the present application the name natural *basis function* seems preferable over the more usual name natural *pixel*. Furthermore, the name natural basis function stresses the relation with local and global basis functions. The strong variation within the strip may give rise to unwanted effects in reconstructions, in particular when neighbouring channels do hardly overlap. In such a case, the support NBFs (i.e. the support of K; $J = I$) may be preferable [Fig.2(b)]:

$$B^2_{jm} = \begin{cases} 1 & \text{if } K_{jm} > 0, \\ 0 & \text{if } K_{jm} = 0. \end{cases} \tag{14}$$

Regular NBFs are obtained by defining the geometric matrix K' of an alternative regular viewing geometry, for example parallel beams at regular angles. For regular constant NBFs B^3 [Fig.2(c)] parallel strips with constant values were taken, whereas for regular triangular NBF B^4 [Fig.2(d)] parallel strips overlapping halfway with their neighbours and having triangular values over the width were chosen. Note that in this case I and J need not be identical, although they will be chosen to be close. It is evident that all NBFs defined so far are highly non-orthogonal. Given the singular value decomposition (SVD) $K = U_K S_K V_K^{\mathsf{T}}$, the subscripts indicating the matrix of which the SVD matrices are the decomposition, orthonormal NBFs can be obtained by taking [18]

$$B^5 = \left[(S_K S_K^{\mathsf{T}})^{+} \right]^{1/2} S_K V_K^{\mathsf{T}}, \tag{15}$$

where the plus sign indicates the Moore-Penrose pseudo-inverse (see section 2.4). The basis functions of Eq.(15) (rows of B^5; $J = I$) basically correspond to the first I rows of V_K^{T}, which are orthonormal. Contour plots of two typical orthonormal NBFs for the JET SXR system are given in Fig.2(e,f). The structure of these NBFs for the SXR system is not very clear, although many contours are spread along one or more lines of sight. For a system with regular coverage much more structure can be expected [18].

Two sets of LBFs (with $J \approx I$) have been constructed to make possible a direct comparison of NBFs with LBFs. These LBFs are non-overlapping square constant pixels B^6 [Fig.2(g)] and half-overlapping "pyramid" basis functions B^7 [Fig.2(h)]. The latter are the product of one triangle function in the Z (or y) direction and one in the R (or x) direction [11], which results in a pyramid shape with rounded corners. The summation of Eq.(1) in the case of the pyramid LBFs results in a continuous $g(x,y)$, whereas in the case of the square constant pixels $g(x,y)$ is step-like. A summary of the NBFs and LBFs used in this report is given in Table I.

Table I: Summary of the basis functions used.

Name	Type	Definition	Eq.
B^1	standard NBF	$B^1=K$	13
B^2	support NBF	$B^2_{jm} = \begin{cases} 1 & \text{if } K_{jm} > 0, \\ 0 & \text{if } K_{jm} = 0. \end{cases}$	14
B^3	regular constant NBF (generalized)	constant value within regularly spaced strips	
B^4	regular triangular NBF (generalized)	triangular value within regularly spaced overlapping strips	
B^5	orthonormal NBF	$B^5 = \left[(S_K S_K^{\mathsf{T}})^+\right]^{1/2} S_K V_K^{\mathsf{T}}$	15
B^6	square constant LBF	constant within square	
B^7	pyramid LBF	product of two overlapping triangle functions in x and y directions	

Figure 2(a) makes clear that the matrix K has very few non-zero elements (a couple of per cent), and that consequently the matrices B in all cases, except for the orthonormal basis functions, do so as well. Because M is chosen large (typically 400×800) it was necessary to store and use only the non-zero elements of these matrices to limit the use of memory and to speed up the calculation of the projection-backprojection matrix A.

2.4 Inversion

The tomography problem without *a priori* information can be stated as follows: given $\boldsymbol{f}$, invert Eq. (3) to give $\tilde{\boldsymbol{g}}$ and then backproject this with Eq.(1) to obtain the local emissivity values that

can be represented in graphical form. Because the tomographic inversion problem is ill-posed, a regularized inversion method is needed. Truncated SVD (TSVD) is a reasonable way to obtain a stable solution to Eq.(3) when $J \approx I$ (see for instance Ref.15 and references therein, and Ref.20). The (truncated) pseudo-inverse or Moore-Penrose inverse of the $I \times J$ matrix A, with SVD $A = U_A S_A V_A^{\mathsf{T}}$, is given by [22]

$$A^{+} = V_A S_A^{+} U_A^{\mathsf{T}}, \tag{16}$$

where S_A is a $I \times J$ diagonal matrix $S_A = \mathrm{diag}(s_1, \mathrm{K}, s_r)$, with $r = \min(I, J)$ and singular values $s_1 \mathrm{K}\ s_r$, and its pseudo-inverse is the diagonal $J \times I$ matrix $S_A^{+} = \mathrm{diag}(1/s_1, \mathrm{K}, 1/s_t, 0, \mathrm{K}, 0)$, with truncation value $t \le \mathrm{rank}(A) \le r$. The singular values are customarily sorted in descending order. Small singular values will make the inverse A^{+} unstable; this can be prevented by truncating the inverse, i.e. by choosing t suitably ($t < r$). It can be shown that the solution $\tilde{\boldsymbol{g}} = A^{+}\boldsymbol{f}$ is the least square solution if the system is overdetermined ($I \ge J$) and the minimum norm solution if the system is underdetermined ($I < J$) [22].

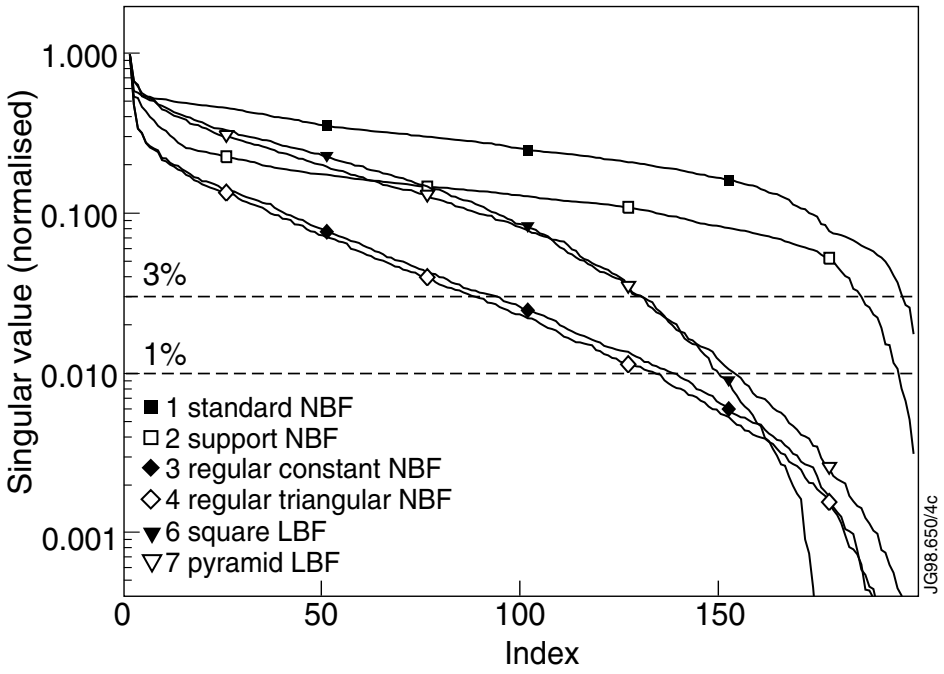

Fig.3: Singular values of the projection-backprojection matrix A *for the JET SXR system, normalized to the largest singular value. These singular values were obtained with* K *on the fine 400×800 grid.*

Figure 3 shows the singular values of the projection-backprojection matrix for the various basis functions for the JET SXR system. The characteristics of all NBFs and LBFs are similar: the first few singular values drop quickly, then there are more than a hundred singular values with constant slope (on a logarithmic scale) and above about 160 the values drop steeply. Small singular values, in particular after the steep drop, indicate redundancy in the information about the emission profile by the basis functions (the redundancy is due to the overlap in the support of geometric functions corresponding to crossing the lines of sight). Apparently, there is less

redundancy in the standard and support NBFs (B^1 and B^2) than in the other NBFs and LBFs. The singular values of the orthonormal B^5, i.e. the singular values of K, are not shown; their relation to the singular values of standard NBFs is discussed later. The truncation of the SVD should be done before the singular values fall off below the noise level; the optimal choice of truncation will be discussed in connection with the simulations in section 3.1. The number of singular values of the matrix A that can be taken in the TSVD corresponds to the degrees of freedom, or independent pieces of information, gathered by the measuring system [13].

The SVD of A can be calculated by standard mathematical packages. It is computationally intensive, but for given K and B it only needs to be done once and the matrices U_A, S_A and V_A can be stored. For standard and orthonormal NBFs more can be said because of the way K and A are related.

For standard NBFs ($B^1 = K$), $A = KK^{\mathsf{T}}$ is symmetric and its SVD is

$$A = U_A S_A V_A^{\mathsf{T}} = U_K S_K S_K^{\mathsf{T}} U_K^{\mathsf{T}}. \tag{17}$$

Here, the unitary properties of U and V were used. It follows from Eq.(17) that the singular values of A are those of K squared. With the SVD of K, it is easy to show that backprojection of $\tilde{\boldsymbol{g}} = A^{+}\boldsymbol{f}$ with Eq. (11) gives the trivial result

$$\boldsymbol{g} = K^{+}\boldsymbol{f}. \tag{18}$$

The solution found with standard NBFs is therefore equal to the solution found if TSVD were applied to K in Eq. (12). Equations equivalent to Eq. (18) for solving $\boldsymbol{g}$ are $\boldsymbol{g} = K^{\mathsf{T}}\left(KK^{\mathsf{T}}\right)^{+}\boldsymbol{f}$ and $\boldsymbol{g} = \left(K^{\mathsf{T}}K\right)^{+}K^{\mathsf{T}}\boldsymbol{f}$, which numerically can give slightly different results [15]. The application of standard NBFs has some advantages over the direct application of TSVD to Eq.(12). (1) If the function $K_i(x,y)$ can be expressed analytically, the continuous backprojection of the inversion of Eq.(3) is likely to be more accurate than a discretization of $\boldsymbol{g}$ and K on a grid and then solving by Eq.(18) [14,15]. (2) If the number of grid basis functions required for an accurate discretization of $\boldsymbol{g}$ and K is larger than the number of measurements, SVD of A is more efficient than SVD of K; hence the NBF approach is more efficient than the solution of solution of Eq.(18). (3) If the coverage of the measuring system is regular, A has a structure [14] that one can take advantage of in the calculation of the SVD [18]. In the present application, only point 2 is applicable.

Using B^5 of Eq. (15) in Eq. (3) and substitution into Eq. (11) also leads to Eq. (18), showing that orthonormal NBFs are not very different from standard NBFs. The results in Ref. 18 confirm this; there the inversion formula $\boldsymbol{g} = K^{\mathsf{T}}\left(KK^{\mathsf{T}}\right)^{+}\boldsymbol{f} = K^{\mathsf{T}}U_K\left(S_K S_K^{\mathsf{T}}\right)^{+}U_K^{\mathsf{T}}\boldsymbol{f}$ was used. The orthonormal NBFs are therefore not considered any further in this report. However, in certain applications orthonormal NBFs can be useful [18]. Furthermore, the orthonormal NBFs give insight into what the actual basis functions are when one solves Eq.(12) by means of the TSVD of Eq.(18).

2.5 Constrained-optimization method

The performance of tomography methods can be compared by means of phantom simulations. Phantoms are assumed emission profiles, which are used to calculate pseudo-measurements, i.e. what the detectors would measure if the phantom were the true emission profile. The tomographic reconstruction of the pseudo-measurements, which is often called tomogram, can be compared with the phantom. The NBF and LBF methods described are compared in phantom simulations with the standard tomography method used for SXR and bolometer tomography at JET [11], which is here referred to as the *reference* method. This is a series-expansion method with a grid of pyramid LBFs (there are about six times more basis functions than measurements) in which the solution is found by a constrained optimization (this is equivalent to Phillips-Tikhonov regularization). The *a priori* information is given by an object function that quantifies anisotropic smoothness on flux surfaces [11,23], in other words: for the given constraints the smoothest solution is found. From the tomogram one can also backcalculate what would be measured if the tomogram were the actual emission profile and compare these with the pseudo-measurements from the phantom. This gives the misfit σ_f between (pseudo) measurements f_0 and backcalculated measurements f:

$$\sigma_f = \frac{\|f - f_0\|}{\|f_0\|}, \tag{19}$$

where the bars indicate the Euclidean norm. The constraint in the constrained optimization method is given by the so-called discrepancy principle [24], i.e. the solution is found for which the misfit equals the estimated errors ε in the measurements. The main parameter in the constrained optimization method is given by the estimated errors; other parameters specify the exact form of the object function. Other, similar tomography methods applied to SXR tomography, and tomography in other wavelength ranges on fusion devices, often use square pixel basis functions, and isotropic smoothness, flatness or maximum entropy as object function [5,8–10,25,26].

3. COMPARISON OF TOMOGRAPHY METHODS

3.1 Description of simulations

In the numerical implementation of the tomography methods two types of local basis functions $b_m(x,y)$ have been used. The first type consists of 400×800 square pixels and will be referred to as the fine grid. This grid was chosen sufficiently fine so that the geometric functions $K_i(x,y)$ could be accurately represented. The tomograms are shown on this grid. An efficient way to calculate the discrete representation of $K_i(x,y)$ is discussed Ref.3. Such a fine grid was feasible in the TSVD methods on the (nearly) square matrix A, of which the dimensions are equal to the number of measurements. However, in the constrained-optimization method a square matrix related to $K^{\mathsf{T}}K$ [11], of which the dimensions are equal to the number of basis functions M, is inverted. This inversion requires computer memory that goes as M^2, and the computation time

goes as M^3. Also in the method of TSVD of the matrix *K* the number of grid basis functions (*M*) is the limiting factor. For these two methods the reconstruction is done on a much coarser grid with about 1200 pyramid basis functions (as explained in Sec.2.5), referred to as coarse grid. In this case the discrete representation of $K_i(x,y)$ is an average weighted by the basis functions according to Eq.(9). These representations are not necessarily worse than the fine grid as the phantom is given on the coarse grid. However, it is found (Sec.3.2) that for the LBF and NBF reconstructions the fine grid gives reconstructions closer to the phantom than the coarse grid, which means that for those methods the fine grid is more adequate.

In the simulation a realistic level of noise is added to the pseudo-measurements; in the present simulations that is Gaussian noise with a standard deviation of 3% relative to the pseudo-measurement. Tomographic reconstructions *g* (the tomogram) of the pseudo-measurements can be compared directly with the phantom g_0 to give the tomogram error

$$\sigma_g = \frac{\|g - g_0\|}{\|g_0\|}.$$

The tomogram error is an objective quality measure, with a global minimum, that can be optimized by varying the reconstruction parameters, i.e. the estimated misfit ε in constrained optimization or the number of singular values (expressed in relative terms by s_t/s_1) in TSVD. The misfit σ_f [Eq. (19)] is also a quantitative error measure. Contrary to σ_g it is usually a monotonic function of the estimated misfit ε in constrained optimization or the number of singular values in TSVD. Figure 4 shows that for most methods σ_g has a minimum for a value of ε or s_t/s_1 close to the noise level. The corresponding σ_f of this minimum (Tables II and III) is also expected to be close to the noise level of the measurements. In TSVD σ_f can often be made zero by not truncating at all, which obviously does not give reasonable results as the noise of the measurements is amplified in the reconstruction. Figure 5 gives a typical example of the fit to the pseudo-measurements of the backcalculated values from the tomograms with minimum σ_g. Other objective quality measures, such as the amount of negative values in the tomogram (all tomography methods used in this report can result in unphysical negative emissivity values), could be used. The image of the tomogram also gives an impression of the quality of the reconstruction. Although this is not an objective quality measure, it can play an important role in deciding which method gives the best results.

It is well known that [19] the minimum σ_g in constrained-optimization methods that use the discrepancy principle is often for an ε that is slightly smaller than the noise level [Fig.4(a)]. The truncation level s_t/s_1 for which the minimum σ_g occurs for the NBF and LBF methods [Fig.4(b-h)] corresponds roughly to the truncation that one would expect from the singular values (Fig.3): B^1, B^2 and B^5 have singular values that hardly drop below the noise level and therefore the best results are obtained with very little truncation, whereas for B^3, B^4, B^6 and B^7 the

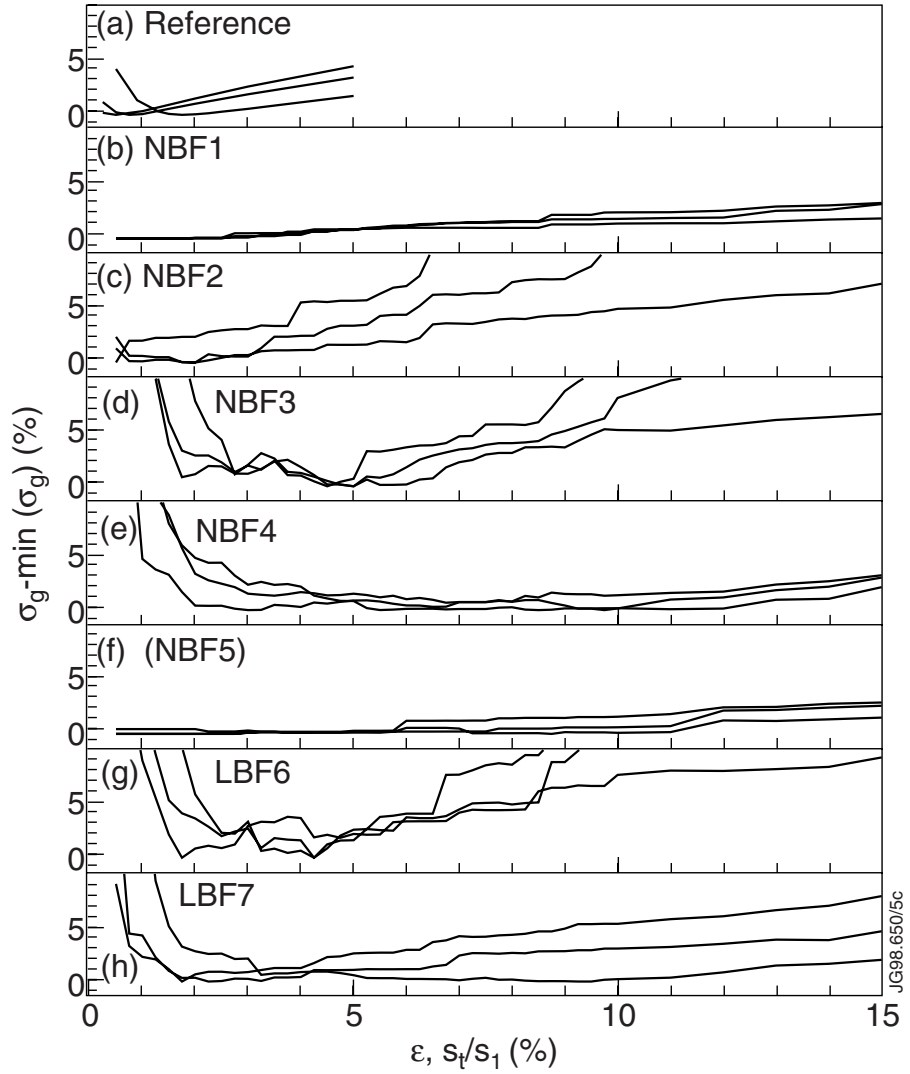

Fig.4: Tomogram errors $\sigma_g - \min(\sigma_g)$ *for three representative phantoms (the three curves in each graph) as a function of* ε *[in (a)] and* s_t/s_1 *[in (b–h)] for tomographic reconstructions on the fine 400×800 grid for the various tomography methods indicated, except (f) which was done by TSVD of the matrix* K *on the coarse grid. The values of* $\min(\sigma_g)$ *can be found in Table II.*

opposite is true. The σ_f for which σ_g is minimum (Tables II and III) is clearly related: for B^1, B^2 and B^5 σ_f is very small (smaller than the noise level), whereas for B^3, B^4, B^6 and B^7 it is close to the noise level, although significant differences occur between phantoms. For each type of basis function the phantom simulations give an indication of the reasonable range of truncation level s_t/s_1 for reconstructions of actual measurements (in which case σ_g cannot be determined as no phantom exists to compare with). Within this range the truncation level can be optimized to give the reconstruction with the least apparent artefacts.

Various phantoms were used in the reconstructions, which are listed in Tables II and III. Phantoms I-III are based on actual measurements reconstructed by the reference method. Because the reference method is known to smooth the result, the peaks of the phantoms were enhanced. Phantoms I [Fig.6(a)] and II are two time slices (JET discharge 40305 at times 13.42 s and

Table II: Tomogram reconstruction errors σ_g (in per cent) and misfit σ_f (within brackets; in per cent) for phantom simulations on the fine grid.

System	Phantom	Reference	NBF 1	NBF 2	NBF 3	NBF 4	LBF 6	LBF 7
JET	I (crescent experim.)	8.0 (2.5)	45.9 (0.0)	34.6 (1.4)	28.4 (2.1)	26.8 (3.5)	28.7 (1.8)	**21.3** (1.8)
JET	II (crescent experim.)	7.0 (2.5)	44.2 (0.0)	31.3 (1.7)	24.4 (3.4)	23.1 (2.6)	25.6 (1.8)	**18.2** (2.0)
JET	III (peaked experim.)	11.4 (3.3)	66.4 (0.0)	37.3 (0.1)	37.8 (10.5)	34.5 (11.3)	47.1 (6.1)	**28.8** (1.6)
JET	IV (Gaussian)	3.5 (2.0)	63.9 (0.0)	34.0 (0.2)	22.0 (4.2)	**18.0** (4.1)	41.6 (2.9)	27.1 (1.1)
JET	V (three Gaussians)	8.3 (2.0)	59.7 (0.0)	35.5 (0.3)	31.8 (5.9)	28.2 (5.5)	40.6 (3.1)	**27.4** (1.5)
JET	VI (ring)	27.1 (11.7)	61.5 (0.0)	43.4 (2.6)	40.5 (8.1)	36.7 (7.7)	40.7 (3.0)	**29.0** (1.2)
JET	VII (inv. crescent)	32.3 (6.8)	72.7 (0.0)	52.7 (0.4)	52.8 (1.3)	49.8 (12.9)	54.5 (4.0)	**41.9** (1.2)
JET	VIII (flat)	20.9 (3.0)	66.7 (0.0)	41.5 (0.2)	37.0 (9.6)	**34.3** (9.4)	48.3 (4.2)	37.8 (1.6)
JET	IX[a]	17.1 (2.6)				10.6 (2.4)		
6×40	I	9.1 (2.8)	23.6 (0.2)	22.7 (3.4)	24.0 (3.1)	22.0 (3.3)	23.3 (3.7)	**17.4** (4.1)
12×40	I	5.5 (3.0)	17.8 (0.5)	16.5 (5.5)	21.1 (6.5)	19.7 (6.0)	21.5 (5.3)	**15.9** (5.3)
6×40	I[b]					20.6 (3.5)		**18.5** (2.7)

[a]Phantom was tomogram of reconstruction with NBF 4 of phantom I.
[b]Basis functions of 12×40 system used, i.e. twice the number of functions normally used.

13.3 s into the discharge, respectively) in a plasma where the toroidal rotation velocity (of the order of 500 km s^{-1}) varies with time. Impurities accumulate in the plasma, but they do not necessarily reach the centre on a short time scale. The centrifugal force from the toroidal plasma rotation can cause an in-out asymmetry in the impurity density that shows up as a crescent-shaped emission profile (see references in Ref.[11]). The radiation by the impurity ions can be as large as the background bremsstrahlung and recombination radiation. Phantom III is based on an optimized-shear discharge [27] (JET discharge 40554 at 7.08 s into the discharge), in which the density and temperature profiles, and hence the SXR emission profile, are strongly peaked in the centre. Phantoms IV–VIII are mathematical inventions that are not likely to occur in a plasma,

Table III: Tomogram reconstruction errors σ_g (in per cent) and misfit σ_f (within brackets; in per cent) for phantom simulations on the coarse grid.

System	Phantom	Ref.	NBF 1	NBF 2	NBF 3	NBF 4	(NBF 5)	LBF 6	LBF 7
JET	I	8.0 (2.5)	33.8 (1.0)	35.5 (2.7)	34.3 (2.8)	36.8 (4.7)	33.8 (1.0)	35.7 (1.5)	**25.9** (2.1)
JET	II	7.0 (2.5)	30.7 (0.8)	32.3 (2.7)	30.1 (2.6)	32.9 (3.7)	30.7 (0.8)	33.5 (1.7)	**22.9** (2.1)
JET	III	11.4 (3.0)	49.1 (0.0)	43.2 (3.4)	46.7 (10.3)	41.8 (11.1)	49.1 (0.0)	47.7 (4.2)	**28.7** (1.6)
JET	IV	3.5 (2.0)	46.5 (0.0)	40.8 (2.9)	28.1 (4.2)	**25.6** (4.1)	46.5 (0.0)	40.4 (2.4)	26.9 (1.2)
JET	V	8.3 (2.0)	45.6 (0.3)	40.3 (2.2)	40.9 (4.9)	37.9 (5.6)	45.6 (0.3)	42.0 (2.4)	**28.3** (1.5)
JET	VI	27.1 (11.7)	45.2 (0.0)	41.3 (2.8)	46.7 (7.1)	46.6 (8.7)	45.2 (0.0)	48.5 (1.7)	**29.5** (1.3)
JET	VII	32.3 (6.8)	58.9 (0.0)	51.5 (3.1)	62.2 (13.8)	61.0 (13.5)	58.9 (0.0)	61.0 (3.1)	**42.8** (1.2)
JET	VIII	20.9 (3.0)	52.5 (0.0)	50.0 (5.0)	44.9 (10.3)	44.4 (9.6)	52.5 (0.0)	53.7 (2.5)	**42.7** (1.5)
6×40	I	9.1 (2.8)	24.6 (1.0)	26.8 (4.4)	30.9 (4.1)	35.5 (10.9)	24.6 (1.0)	28.6 (3.3)	**23.0** (2.9)
12×40	I	5.5 (3.0)	23.1 (4.6)	**18.2** (4.2)	27.2 (4.2)	34.0 (12.1)	23.1 (4.6)	44.3 (6.2)	24.0 (6.2)

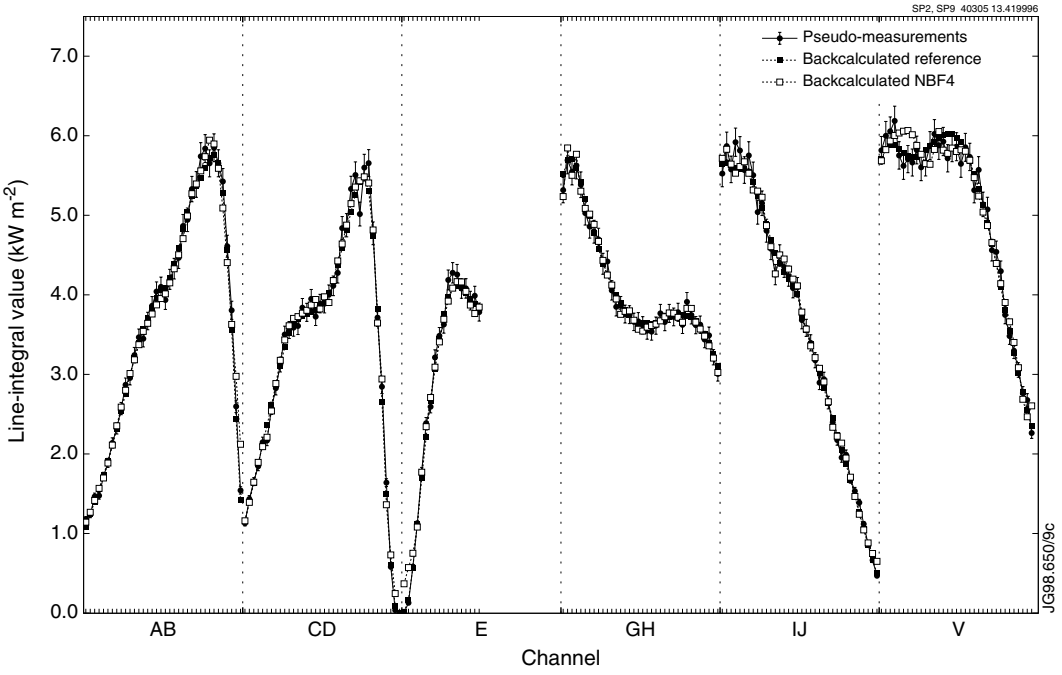

Fig.5: Pseudo-measurements for phantom I (the error bars indicate the standard deviation of the added noise) and backcalculated values for the reference method and the method with NBF 4, for all detectors of the JET SXR system.

but that give insight into what happens if there are multiple peaks or very steep gradients in the emission profile. Phantom IV is a Gaussian emission profile, V consists of three Gaussians, VI is a ring with a Gaussian cross-section, VII is similar to VI but with an angular variation that peaks on the inside, and VII is a circle with unity emission inside and zero emission outside. The reconstruction errors in Tables II and III show that results of the various phantoms are the same qualitatively, i.e. the relative performance of the various tomography methods does not depend much on the phantom. Therefore, only tomograms of the phantom simulations with phantom I are discussed in detail (Fig.6).

3.2 Simulation results

The reconstructions shown in Fig.6 were all done on the fine grid, except the reference case [Fig.6(b)] and the TSVD of matrix K [Fig.6(h)]. The corresponding reconstruction errors are given in Table II. Figure 6(b) shows that the reference method gives a reconstruction that is very similar to the phantom [Fig.6(a)], but that the peak and the hollow have been somewhat smoothed, as can be expected when using a regularization based on smoothness. The NBFs B^1 [Fig.6(c)] do not give good reconstructions, with high values at the edge, because the basis functions have a triangular shape and neighbours do not overlap. Still, the crescent shape is discernible. The NBFs B^2 [Fig.6(d)] perform better because the supports of the geometric functions of the detectors of a camera fill the region well. However, due to the irregular coverage by the system, one gets unrealistic gaps between viewing directions. The NBFs B^3, which correspond to a virtual system with regular coverage, alleviate this problem and the reconstruction is better [Fig.6(e)]. The "cubist" features of the reconstruction, i.e. sharp edges, can be rounded by smoothing the image, which gives a very acceptable result [Fig.6(f)]. A smooth result is also obtained by using triangular regular NBFs [B^4, Fig.6(g)], which give the best result of the types of NBF tested. Straightforward TSVD of the matrix K on the coarse grid, which mathematically corresponds to the orthonormal NBFs B^5, also leads to a reasonable reconstruction [Fig.6(h)], but of a lesser quality than obtained with the reconstructions on the fine grid (cf. Table II and Table III). The reconstruction with square LBFs B^6 [Fig.6(i)] also shows the main features, but for all phantoms the reconstruction is worse than that with NBFs B^3 and B^4, and often worse than reconstructions with NBFs B^2. This is in agreement with what has been found in the literature [14,15]. The smoother reconstruction with pyramid LBFs B^7 [Fig.6(j)] is better. In fact, its tomogram error is lower than for any of the NBFs for most phantoms. The relatively large size of the basis functions is clear from the many local minima and maxima. Although the reconstructions with NBF B^4 are not free from artefacts, they seem preferable to the reconstructions with B^7 despite the somewhat larger tomogram error, in particular because the hollowness and values on the left side of the crescent are reconstructed better and because the tomogram is smoother. The reason for the tomogram error being larger for the NBFs is probably that there are non-zero features at the edge of the plasma, while such features are suppressed for LBF B^7 because the basis functions go to zero in many places close to the edge.

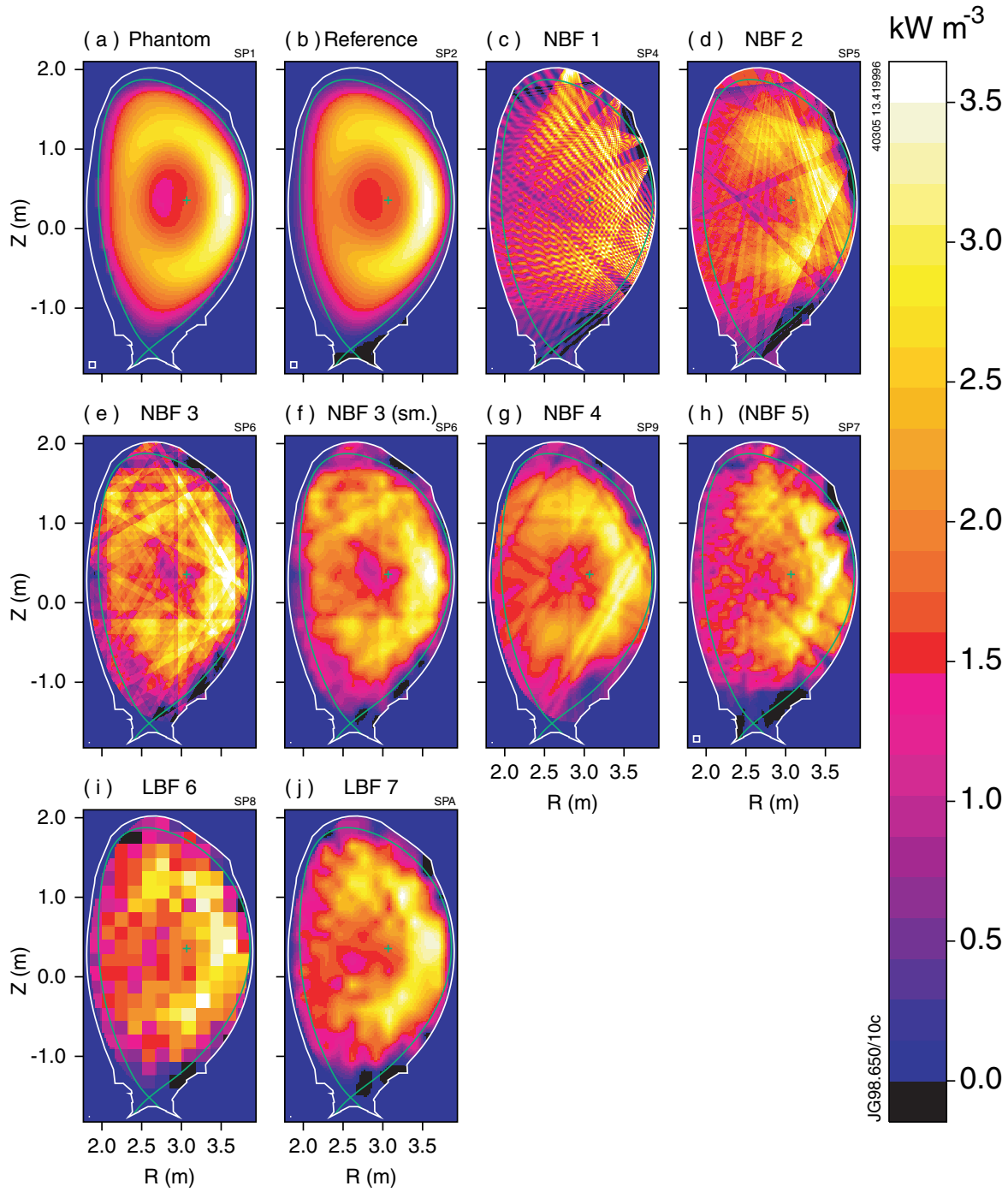

Fig.6: (a) Phantom I. Tomographic reconstructions by the various methods: (b) reference method, (c–g) NBFs, (h) TSVD of the matrix K *on the coarse grid and (i,j) LBFs. Image (f) was derived from image (e) by smoothing. The green curve indicates the magnetic separatrix in the plasma and the box in the lower left corner the grid size.*

On may argue that the comparison with the reference method for phantoms I–III is unfair, as the phantom is based on a reconstruction by this method and thus is smooth. If a less smooth phantom is used that does not satisfy the *a priori* information in the reference method, in particular the tomogram of the reconstruction with NBF B^4 (phantom IX in Table II), the reconstruction with the reference method has a significantly higher reconstruction error than the reconstruction with NBF B^4. Thus, it can be concluded that the excellent results with the reference method are

biased by the smooth phantoms used. If the emission profile is particularly suited for a NBF method, the reconstruction can be better than with the reference method. However, the unsmooth features in reconstructions with NBF methods are mainly artefacts of the basis functions used. Therefore, for reconstructions of actual emission profiles of the plasma one can expect the reference method to perform a little worse than in the phantom simulations, but still to be much better than the NBF and LBF methods without *a priori* information.

Table III summarizes the simulation results on the coarse grid. These result are less good than those on the fine grid (Table II), thus it can be concluded that the coarse grid may not be sufficiently fine to accurately describe the basis functions in numerical terms.[6] This may be the cause of the trends in the simulations on the coarse grid being less clear when comparing phantoms, although again the LBFs B^7 perform best for most phantoms. The simulations on the coarse grid have been useful, however, to numerically verify that the results with NBF B^1 and NBF B^5 are be identical, as discussed in section 2.4. This is indeed the case (see Table III): the optimum reconstruction error is found for the same number of singular values (note however that s_t/s_1 of NBF B^1 is s_t/s_1 of NBF B^5 squared).

Some of the artefacts in Figs.6(c-g) can clearly be attributed to the irregular coverage of the channels and the shapes of the geometric functions. One can therefore ask, whether better results can be obtained with NBFs if the coverage is more regular. One can also wonder whether the good performance of NBFs reported in the literature is due to the much larger number of channels in those applications. To address the first question, simulations have been carried out with a virtual system with approximately the same number of channels as the JET SXR system, but spaced in a regular way: six fans at regular angles with 40 channels each, where each fan covers the entire plasma cross-section [solid lines in Fig.1(b)]. To address the second question, six additional virtual fans were added on the low-field side of the tokamak vessel to give a total of 12x40 channels [solid and dashed lines in Fig.1(b)]. Because the qualitative results for the various phantoms in the simulations with the JET SXR system were the same, the simulations with the virtual systems were only carried out for phantom I. The number of NBFs B^3 and B^4, and LBFs B^6 and B^7 was increased according to the number of channels available in the virtual systems. The results are given in Table II. Surprisingly, the reconstruction with the reference method for the 6×40 system is somewhat worse than that with the JET SXR system. The reconstruction for the 12×40 system, however, is significantly better. It is clear that the NBF methods perform much better with the regular systems. For the 12×40 system NBFs B^1 and B^2 even outperform NBFs B^3 and B^4, indicating that (1) the problems for the JET SXR system

6 With the phantom given on the coarse grid, pseudo-measurements calculated by the geometric matrix on the fine and the coarse grids are identical (within 0.001%). Therefore, discretization errors of the geometric matrix on the coarse grid are not to blame for the worse performance of NBF and LBF methods on the coarse grid: for a phantom on the coarse grid the reference method can be expected to give identical results on the fine and coarse grids (but the reconstruction on the coarse grid would take of the order 10^7 times longer and require of the order 10^5 times more memory).

were purely due to limitations in that system and (2) for regular systems it is better to use normal NBFs based on the geometric function than generalized NBFs based on a virtual regular system. However, the LBFs also perform better for the regular systems and the tomogram errors for LBFs B^7 are still somewhat better than the tomogram errors with NBFs. The singular values of the 6×40 system show a constant slope and no severe drop off which indicates that the system is more balanced than the irregular JET SXR system. The first 240 singular values of 12×40 system are similar to the ones of the 6×40 system; the singular values drop off later. This indicates that there is a growing redundancy with more channels, which is typical for tomography (an asymptotic limit is reached in the degrees of freedom as number of views increases [13]). A test was done by reconstructing the measurements of the 6×40 system using the NBFs B^4 and LBFs B^7 of the 12×40 system (bottom row of Table II), i.e. there were twice as many basis functions as there are measurements. The results show that not much is gained by using more basis functions than measurements (if no extra *a priori* information is applied): the reconstruction with NBFs B^4 is only slightly better and the reconstruction with LBFs B^7 is worse.

4. CONCLUSIONS

Natural basis functions have been applied successfully to tomography with the JET SXR system in numerical simulations. Although reconstructions with a conventional tomography method are significantly better, reconstructions with NBFs, which require less *a priori* information than the conventional tomography methods, are useful to investigate whether features of a reconstruction are real or may be due to the regularizing *a priori* information in conventional tomography methods. An application of the NBF methods for this purpose is discussed in Ref. 28. Apparently, the information supplied by the number of measurement of the JET SXR system is sufficient to derive the main features of the emission profiles. Simulations with virtual systems with improved coverage and a doubled number of detectors show that significantly improved reconstructions can be obtained with such systems, but that the conventional tomography method remains preferable.

If the coverage by the viewing system is irregular, the regular (generalized) NBFs perform better than the NBFs that describe the actual viewing system. For systems with regular coverage and optimum overlap between neighbouring channels the opposite is true. The appropriate NBFs give more accurate reconstructions than the traditional pixels (LBFs without *a priori* information). Pyramid LBFs, which describe a bilinear interpolation between grid points, give smaller reconstruction errors than NBFs for most phantoms. However, the reconstructions with pyramid LBFs have coarse artefacts, and the smoother reconstructions obtained by NBFs, which show some relevant features better, may be preferable. The larger reconstruction errors in the latter may be due to relatively larger artefacts at the edge of the reconstruction region. It is possible to improve the generalized-NBF reconstructions by including *a priori* information, such as

smoothness between virtual lines of sight of the basis functions and small values for edge lines of sight, but this is outside the scope of this report in which an attempt is made to minimize the influence of *a priori* information. Other types of NBFs than those discussed here have been proposed in the literature, such as weighted NBFs [29], multigrid NBFs [30] and multiscale NBFs [31]. The application of such NBFs to the present SXR tomography problem may be studied in the future.

REFERENCES

[1] R.M. Lewitt, "Reconstruction algorithms: transform methods," *Proc. IEEE* **71**, 390–408 (1983)

[2] L.C. Ingesson and V.V. Pickalov, "An iterative projection-space reconstruction algorithm for tomography systems with irregular coverage," *J. Phys. D: Appl. Phys.* **29**, 3009–3016 (1996)

[3] L.C. Ingesson, P.J. Böcker, R. Reichle, M. Romanelli and P. Smeulders, "Projection-space methods to take into account finite beam-width effects in two-dimensional tomography algorithms," *J. Opt. Soc. Am. A* **16**, 17–27 (1999)

[4] K.M. Hanson and G.W. Wecksung, "Local basis-function approach to computed tomography," *Appl. Opt.* **24**, 4028–4039 (1985)

[5] S. Zoletnik and S. Kálvin, "A method for tomography using arbitrary expansions," *Rev. Sci. Instrum.* **64**, 1208–1212 (1993)

[6] R.S. Granetz and P. Smeulders, "X-ray tomography at JET," *Nucl. Fusion* **28**, 457–476 (1988)

[7] Y. Nagayama, "Tomography of m=1 mode structure in tokamak plasma using least-square-fitting method and Fourier-Bessel expansion," *J. Appl. Phys.* **62**, 2701–2706 (1987)

[8] A. Holland and G.A. Navratil, "Tomographic analysis of the evolution of plasma cross sections," *Rev. Sci. Instrum.* **57**, 1557–1566 (1986)

[9] N. Iwama, H. Yoshida, H. Takimoto, Y. Shen, S. Takamura and T. Tsukishima, "Phillips-Tikhonov regularization of plasma image reconstruction with the generalized cross validation," *Appl. Phys. Lett.* **54**, 502–504 (1989)

[10] J. Mlynář , "Pixels method computer tomography in polar coordinates," *Czech. J. Phys.* **45**, 799–816 (1995)

[11] L.C. Ingesson, B. Alper, H. Chen, A.W. Edwards, G.C. Fehmers, J.C. Fuchs, R. Giannella, R.D. Gill, L. Lauro-Taroni and M. Romanelli, "Soft x-ray tomography during ELMs and impurity injection in JET," *Nucl. Fusion* **38**, 1675–1694 (1998)

[12] R.M. Lewitt, "Multidimensional digital image representations using generalized Kaiser-Bessel window functions," *J. Opt. Soc. Am. A* **7**, 1834–1846 (1990)

[13] D.G. McCaughey and H.C. Andrews, "Degrees of freedom for projection imaging," *IEEE Trans. Acoustics, Speech, Signal Processing* **ASSP-25**, 63–73 (1977)

[14] M.H. Buonocore, W.R. Brody and A. Macovski, "A natural pixel decomposition for two-dimensional image reconstruction," *IEEE Trans. Biomed. Eng.* **BME-28**, 69–78 (1981)

[15] G.T. Gullberg and G.L. Zeng, "A reconstruction algorithm using singular value decomposition of a discrete representation of the exponential Radon transform using natural pixels," *IEEE Trans. Nucl. Sci.* **41**, 2812–2819 (1994)

[16] G.T. Gullberg, Y.-L. Hsieh and G.L. Zeng, "An SVD reconstruction algorithm using a natural pixel representation of the attenuated Radon transform," *IEEE Trans. Nucl. Sci.* **43**, 295–303 (1996)

[17] Y.-L. Hsieh, G.T. Gullberg, G.L. Zeng and R.H. Huesman, "Image reconstruction using a generalized natural pixel basis," *IEEE Trans. Nucl. Sci.* **43**, 2306–2319 (1996)

[18] J.R. Baker, T.F. Budinger and R.H. Huesman, "Generalized approach to inverse problems in tomography: image reconstruction for spatially variant systems using natural pixels," *Critical Reviews in Biomedical Engineering* **20**, 47–71 (1992)

[19] V.F. Turchin, V.P. Kozlov and M.S. Malkevich, "The use of mathematical-statistics method in the solution of incorrectly posed problems," *Sov. Phys. Usp.* **13**, 681–703 (1971)

[20] P.C. Hansen, "Numerical tools for analysis and solution of Fredholm integral equations of the first kind," *Inverse Problems* **8**, 849–872 (1992)

[21] K.M. Hanson and G.W. Wecksung, "Bayesian approach to limited-angle reconstruction in computed tomography," *J. Opt. Soc. Am.* **73**, 1501–1509 (1983)

[22] G.H. Golub and C.F. Van Loan, *Matrix computations 3rd Ed.* (Johns Hopkins University Press, Baltimore, 1996) pp 256

[23] J.C. Fuchs, K.F. Mast, A. Hermann, K. Lackner, "Two-dimensional reconstruction of the radiation power density in ASDEX Upgrade," *Proceedings of the 21st EPS Conference on Controlled Fusion and Plasma Physics*, Montpellier, 27 June–1 July 1994, Ed. E. Joffrin *et al.*, Europhysics Conference Abstracts Vol. 18B (EPS, 1994), Part III, pp 1308

[24] M. Bertero, C. de Mol and E.R. Pike, "Linear inverse problems with discrete data: II. Stability and regularisation" *Inverse Problems* **4**, 573–594 (1988)

[25] K. Ertl, W. Von der Linden, V. Dose and A. Weller, "Maximum-entropy based reconstruction of soft x-ray emissivity profiles in W7-AS," *Nucl. Fusion* **36**, 1477–1488 (1996)

[26] M. Anton, H. Weisen, M.J. Dutch, W. Von der Linden, F. Buhlmann, R. Chavan, B. Marletaz, P. Marmillod and P. Paris, "X-ray tomography on the TCV tokamak," *Plasma Phys. Control. Fusion* **38** ,1849–1878 (1996)

[27] The JET Team (presented by F.X. Söldner), "Shear optimization experiments with current profile control on JET," *Plasma Phys. Control. Fusion* **29**, B353–B370 (1997)

[28] L.C. Ingesson, H. Chen, P. Helander and M.J. Mantsinen, "Comparison of basis functions in soft x-ray tomography and observation of poloidal asymmetries in impurity density" *Plasma Phys. Control. Fusion* **42**, 161-180 (2000)

[29] L. Garnero, J.-P. Hugonin and N. De Beaucoudrey, “Limited-angle tomographic imaging using a constrained natural-pixel decomposition,” Opt. Acta **33**, 659-671 (1986)

[30] V.E. Henson, M.A. Limber, S.F. McCormick, B.T. Robinson, “Multilevel image reconstruction with natural pixels,” SIAM J. Sci. Computing **17**(1), 193-216 (1996)

[31] M. Bhatia, W.C. Karl, and A.S. Willsky, “Tomographic reconstruction and estimation on multiscale natural-pixel bases,” IEEE Trans. Image Proc. **6**(3), 463-478 (1997)